

Atomic bound state and scattering properties of effective momentum-dependent potentialsGautham Dharuman,¹ John Verboncoeur,^{1,2} Andrew Christlieb,^{2,3} and Michael S. Murillo^{4,5}¹*Department of Electrical and Computer Engineering, Michigan State University, East Lansing, Michigan 48824, USA*²*Department of Computational Mathematics, Science and Engineering, Michigan State University, East Lansing, Michigan 48824, USA*³*Department of Mathematics, Michigan State University, East Lansing, Michigan 48824, USA*⁴*New Mexico Consortium, Los Alamos, New Mexico 87544, USA*⁵*Computational Physics and Methods Group, Los Alamos National Laboratory, Los Alamos, New Mexico 87544, USA*

(Received 1 June 2016; published 24 October 2016)

Effective classical dynamics provide a potentially powerful avenue for modeling large-scale dynamical quantum systems. We have examined the accuracy of a Hamiltonian-based approach that employs effective momentum-dependent potentials (MDPs) within a molecular-dynamics framework through studies of atomic ground states, excited states, ionization energies, and scattering properties of continuum states. Working exclusively with the Kirschbaum-Wilets (KW) formulation with empirical MDPs [C. L. Kirschbaum and L. Willets, *Phys. Rev. A* **21**, 834 (1980)], optimization leads to very accurate ground-state energies for several elements (e.g., N, F, Ne, Al, S, Ar, and Ca) relative to Hartree-Fock values. The KW MDP parameters obtained are found to be correlated, thereby revealing some degree of transferability in the empirically determined parameters. We have studied excited-state orbits of electron-ion pair to analyze the consequences of the MDP on the classical Coulomb catastrophe. From the optimized ground-state energies, we find that the experimental first- and second-ionization energies are fairly well predicted. Finally, electron-ion scattering was examined by comparing the predicted momentum transfer cross section to a semiclassical phase-shift calculation; optimizing the MDP parameters for the scattering process yielded rather poor results, suggesting a limitation of the use of the KW MDPs for plasmas.

DOI: [10.1103/PhysRevE.94.043205](https://doi.org/10.1103/PhysRevE.94.043205)**I. INTRODUCTION**

Large-scale simulations are needed to model nonequilibrium electronic dynamics in a wide variety of scenarios, including stopping power experiments in dense plasmas [1,2], multispecies mixing under extreme conditions [3,4], nonequilibrium x-ray Thomson scattering (XRTS) [5,6], laser-matter experiments (e.g., core ionization in x-ray free electron laser experiments [7,8]), and ultracold neutral plasmas [9]. The need for such modeling stems from the emergence of recent large-scale experimental facilities, such as the Z machine [10,11], National Ignition Facility [12,13], Linac Coherent Light Source [14,15], and Deutsches Elektronen-Synchrotron (DESY) [16,17], to name a few. Further, diagnostic capabilities such as imaging XRTS [18,19] will provide unprecedented information about the dynamical evolution of electronic states in these experiments. Coupled with recent advances in computational power that allows molecular dynamics simulations to span unprecedented length (multitrillion particles) and time scales (pico- to microseconds) [20–25], a detailed knowledge of the nonequilibrium dynamics of such systems is, in principle, obtainable; however, it is currently not possible to perform such large-scale simulations for *electronic* dynamics because of the computational overhead in modeling quantum systems.

Most computational approaches to electronic structure fall into three broad categories. Historically the Car-Parinello (CP) [26] method provided an avenue for coupling an electronic structure calculation to ion dynamics, albeit with a fictitious electron dynamics. Similarly, Born-Oppenheimer Molecular Dynamics (BOMD) [27,28], a limiting case of the CP method for massless electrons, forces the electronic

evolution to track the (potentially nonequilibrium) ion dynamical scales. BOMD can also be approximately extended to some electronic dynamical quantities, such as the AC electrical conductivity in the Kubo-Greenwood formulation [29,30], through the use of the Kohn-Sham orbitals and energy eigenvalues. In all three cases, the true electronic dynamics is not modeled.

Conversely, more direct approaches to dynamical evolution employ Time-Dependent Hartree-Fock (TDHF) [31,32] or Time-Dependent Density Functional Theory (TDDFT) [33,34]. TDDFT has been employed for calculating excitation spectra of atoms and molecules [35,36] and the dynamic structure factor of warm dense matter [37]. Conventionally, for an N particle system, TDDFT has an unfavorable $O(N^3)$ scaling that results in a few seconds per propagation step on a multicore implementation (~ 8000 cores) for a system of a few thousand atoms [38]; thus, TDDFT is currently quite limited to small-scale systems over short times. Moreover, incorporating finite temperature states in TDDFT remains a challenge despite recent progress in this area [39,40].

The complete dynamics of the nonequilibrium electrons is described by a $6N$ -dimensional partial differential equation (PDE) [the complex, time-dependent Schrödinger equation (TDSE) in three spatial dimensions]. Simpler alternative approaches that balance physics fidelity with lower computational cost have also been proposed. The general idea is based on mapping the quantum problem onto a framework computable in terms of a classical approach. Mapping to classical-like dynamics offers the advantage of using classical MD techniques with $O(N)$ or $O(N \log N)$ scaling [41] that enable large-scale simulations of interest [42,43]. There are several avenues for constructing a classical framework [44]

for solving the time-dependent quantum problem. For example, Remacle and Levine [45] construct a classical-like framework based on ordinary differential equations for the occupancies and phases. Similarly, the Gaussian-based time-dependent variational principle [46,47] yields classical-like equations of motion. Alternatively, Schiff and Poirier [48] build an effective Lagrangian method that contains higher-order derivatives, which in turn yields classical-looking equations with extra degrees of freedom [49]. Quantum Statistical Potentials (QSPs) [50–52] and empirical potentials for molecular systems [53] are purely classical in their form, with effective potentials; many of these methods have been reviewed elsewhere [54]. However, the WPMD method has several undesirable properties [47], whereas the QSP method suffers from a reliance on statistical properties (e.g., temperature [52]) not well suited for describing nonequilibrium phenomena.

Here we wish to replace the original TDSE with a smaller computational problem using $6N$ ordinary differential equations. We will employ a Hamiltonian formulation that retains the classical phase space variables, but introduces a momentum-dependent potential (MDP) that contains a nonseparable term to account for quantum commutator and Pauli properties. The MDP method represents the full problem in terms of a well-chosen model and empirical parameters. A “well-chosen” model is one that satisfies as many constraints as possible; here the Hamiltonian formulation was specifically chosen because of its natural classical limit and its conservation properties (as discussed in Sec. II). The empirical parameters to this model must be used to train the model to match a finite (and usually small) set of known properties, preferably from accurate experimental data. For these properties, the MDP model can be considered to be exact. Unfortunately, very few exact dynamical properties for quantum systems are known, and limited training of the MDP parameters is possible. Given that set of parameters, the most important issue is then transferability: do the parameters chosen to match some “exactly known” property also describe those properties for which we have no prior knowledge? In fact, this strategy is similar to other approaches, such as the wave-packet approach of Ref. [55] and the machine learning approach of Ref. [56].

MDPs have been quite successful in atomic [57–60], molecular [61], and nuclear physics [62–65]; however, little work has been done for bulk (plasma-like) systems [66]. In such finite-temperature electronic systems electrons undergo excitation, deexcitation, ionization, and recombination. Therefore, the MDP approach for plasma-like systems needs to be established because the identity of an electron in a nonequilibrium system varies from (1) being in the ground state, (2) being in an excited state, (3) ionizing into the continuum, and (4) performing free-free scattering important to transport processes. Our goal here is to establish the efficacy of the MDP approach for modeling large-scale plasma-like system through a careful examination of these four properties. For simplicity, we utilize the best known MDP, the Kirshbaum-Wilets (KW) MDP [57,58,66–76], which has proven very successful for bound states.

This paper is organized as follows. A general formulation of the Hamiltonian approach is presented for arbitrary pair

MDPs in Sec. II to establish a precise definition of an MDP model and its basic properties. We then examine four basic MDP properties, moving from ground-state energies to excited state properties to ionization energies and, finally, free electron scattering properties. Optimization of ground-state energies is discussed in Sec. III, and transferrability of the parameters to atomic systems not in the training set is tested. Next, we turn to the examination of excited state properties in Sec. IV. The transferability of parameters among the properties is examined by using optimized ground-state properties to predict first and second ionization energies; this is discussed in Sec. V. Free-electron properties are then examined in terms of electron-ion scattering in Sec. VI.

II. EFFECTIVE MANY-BODY HAMILTONIAN FORMULATION

In this section we present the Hamiltonian formulation for a nonseparable MDP of the form $V(\mathbf{r}, \mathbf{p})$ that is otherwise arbitrary, including a discussion of the implied constants of motion that serve as constraints. We assume that the equations of motion derived from this Hamiltonian retain their familiar classical form.

Consider an effective Hamiltonian for a system of N_e electrons and N_i ions of the form

$$H = H_C + H_Q, \quad (1)$$

where H_C is the purely classical contribution, given by

$$H_C = \sum_{i=1}^N \frac{\mathbf{p}_i^2}{2m_i} + \sum_{i<j}^N \frac{Z_i Z_j e^2}{|\mathbf{r}_i - \mathbf{r}_j|}, \quad (2)$$

and H_Q incorporates quantum corrections through interactions of the form

$$H_Q = \sum_{i<j}^N [V_{ij}^H(\mathbf{r}_i - \mathbf{r}_j, \mathbf{p}_i - \mathbf{p}_j) + \delta_{s_i s_j} V_{ij}^P(\mathbf{r}_i - \mathbf{r}_j, \mathbf{p}_i - \mathbf{p}_j)], \quad (3)$$

where $N = N_e + N_i$ is the total number of particles, and i and j are particle indices referring to particles of electron (e) or ion (I) subsystems. $Z_e = -1$ for electron, and Z_I is the nuclear charge. V^H is a general Heisenberg MDP between all particles, and V^P is a general Pauli MDP between identical particles [selected by $\delta_{s_i s_j}$ in Eq. (3) where s_i and s_j are spins of particles i and j , respectively]. V^P prevents two identical particles from occupying the same regions of phase space. It is important to note that the V^H and V^P terms do not correspond to purely kinetic or potential energies, consistent with the usual commutator properties of quantum operators. The form for H_Q is not arbitrary, but should be chosen for stability reasons (mitigating the Coulomb catastrophe) and to have empirical flexibility that allows its parameters to be tuned to experimental values. All forms in use have these two properties.

The Hamilton equations for particle i are given by

$$\frac{d\mathbf{r}_i}{dt} = \frac{\partial H}{\partial \mathbf{p}_i} = \frac{\mathbf{p}_i}{m_i} + \sum_{j \neq i}^N \frac{\partial [V_{ij}^H(\mathbf{r}_i - \mathbf{r}_j, \mathbf{p}_i - \mathbf{p}_j) + \delta_{s_i s_j} V_{ij}^P(\mathbf{r}_i - \mathbf{r}_j, \mathbf{p}_i - \mathbf{p}_j)]}{\partial \mathbf{p}_i}, \quad (4)$$

$$\frac{d\mathbf{p}_i}{dt} = -\frac{\partial H}{\partial \mathbf{r}_i} = -\sum_{j \neq i}^N \frac{\partial}{\partial \mathbf{r}_i} \left[\frac{Z_i Z_j e^2}{|\mathbf{r}_i - \mathbf{r}_j|} \right] - \sum_{j \neq i}^N \frac{\partial [V_{ij}^H(\mathbf{r}_i - \mathbf{r}_j, \mathbf{p}_i - \mathbf{p}_j) + \delta_{s_i s_j} V_{ij}^P(\mathbf{r}_i - \mathbf{r}_j, \mathbf{p}_i - \mathbf{p}_j)]}{\partial \mathbf{r}_i}. \quad (5)$$

We would like to point out that $\dot{\mathbf{r}}_i \neq \mathbf{p}_i$; that is, the velocity is not proportional to the canonical momentum because of the addition of the nonseparable MDP.

An important note is that this framework naturally captures finite temperature aspects through the initial conditions for the phase space coordinates; therefore, this formulation does not suffer from the same issues as TDDFT [39], which neglects natural thermal fluctuations [37].

Constants of motion

Due to the nonseparable terms in the Hamilton equations [Eqs. (4) and (5)] as a result of the MDPs, it becomes necessary to check if the fundamental constants of motion like total energy and total angular momentum are conserved. The equation of motion of any function of phase space coordinates $A(\mathbf{r}_1, \mathbf{p}_1, \mathbf{r}_2, \mathbf{p}_2, \dots, \mathbf{r}_N, \mathbf{p}_N)$ for a N particle system is given by

$$\frac{dA}{dt} = \{A, H\} + \frac{\partial A}{\partial t}, \quad (6)$$

where H is the Hamiltonian of the system as given by Eq. (3) and $\{A, B\}$ denotes the Poisson bracket defined as

$$\{A, B\} = \sum_{i=1}^N \left(\frac{\partial A}{\partial \mathbf{r}_i} \frac{\partial B}{\partial \mathbf{p}_i} - \frac{\partial A}{\partial \mathbf{p}_i} \frac{\partial B}{\partial \mathbf{r}_i} \right). \quad (7)$$

When the function A is the Hamiltonian itself, then the equation of motion is given by $\frac{dH}{dt} = \frac{\partial H}{\partial t}$, since $\{H, H\} = 0$.

If the Hamiltonian is time-independent, $\frac{\partial H}{\partial t} = 0$, resulting in $\frac{dH}{dt} = 0$, that is, a time-independent Hamiltonian even with MDPs is a constant of motion. Therefore, the Hamiltonian with MDPs acts as a conserved energy, making it a useful theoretical concept and an important tool in numerical implementations.

Now, let us consider function A to be the total angular momentum of the system given by

$$\mathbf{L}_T = \sum_{i=1}^N \mathbf{L}_i = \sum_{i=1}^N \sum_{\nu} L_{i\nu} \hat{\nu}, \quad (8)$$

where $L_{i\nu}$ is the ν th component of particle i 's angular momentum $\mathbf{L}_i = \mathbf{r}_i \times \mathbf{p}_i$ with $\nu = (x, y, z)$. Since the total angular momentum is a time-independent quantity, its equation of motion is given by

$$\frac{d\mathbf{L}_T}{dt} = \{\mathbf{L}_T, H\} = \sum_{\nu} \left\{ \sum_{i=1}^N L_{i\nu}, H \right\} \hat{\nu}. \quad (9)$$

If the potential is spherically symmetric in position and momentum space, expanding the Poisson bracket of the x component of the total angular momentum and Hamiltonian gives

$$\begin{aligned} \left\{ \sum_{i=1}^N L_{ix}, H \right\} &= \sum_{i=1}^N \{L_{ix}, H\}, \\ &= \sum_{i=1}^N \left(\frac{p_{yi} p_{zi}}{p_i} \frac{\partial H}{\partial p_i} + \frac{z_i y_i}{r_i} \frac{\partial H}{\partial r_i} - \frac{z_i y_i}{r_i} \frac{\partial H}{\partial r_i} - \frac{p_{yi} p_{zi}}{p_i} \frac{\partial H}{\partial p_i} \right) \\ &+ \sum_{i=1}^N \sum_{j \neq i}^N \left[\frac{p_{zi}(p_{yi} - p_{yj})}{p_{ij}} \frac{\partial H}{\partial p_{ij}} + \frac{z_i(y_i - y_j)}{r_{ij}} \frac{\partial H}{\partial r_{ij}} - \frac{p_{yi}(p_{zi} - p_{zj})}{p_{ij}} \frac{\partial H}{\partial p_{ij}} - \frac{y_i(z_i - z_j)}{r_{ij}} \frac{\partial H}{\partial r_{ij}} \right]. \end{aligned} \quad (10)$$

There are some obvious cancellations due to terms of equal and opposite sign resulting in

$$\left\{ \sum_{i=1}^N L_{ix}, H \right\} = \sum_{i=1}^N \sum_{j \neq i}^N \frac{1}{p_{ij}} \frac{\partial H}{\partial p_{ij}} (p_{zj} p_{yi}) + \sum_{i=1}^N \sum_{j \neq i}^N \frac{1}{p_{ij}} \frac{\partial H}{\partial p_{ij}} (-p_{zi} p_{yj}) + \sum_{i=1}^N \sum_{j \neq i}^N \frac{1}{r_{ij}} \frac{\partial H}{\partial r_{ij}} (z_j y_i) + \sum_{i=1}^N \sum_{j \neq i}^N \frac{1}{r_{ij}} \frac{\partial H}{\partial r_{ij}} (-z_i y_j). \quad (11)$$

Since $p_{ij} = p_{ji}$, the first and second terms cancel each other. Similarly, $r_{ij} = r_{ji}$ results in the third and fourth terms canceling each other. Therefore,

$$\left\{ \sum_{i=1}^N L_{ix}, H \right\} = 0. \quad (12)$$

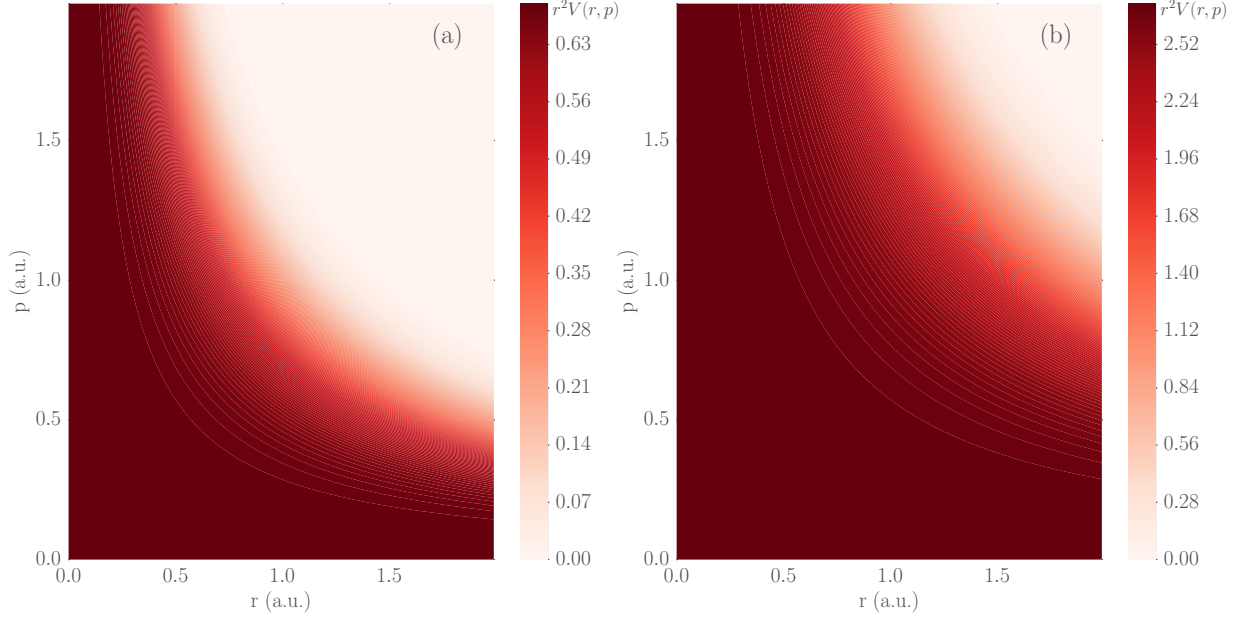


FIG. 1. Plots of $r^2[V(r, p) = \frac{\varepsilon^2}{4\alpha r^2} e^{\alpha[1-(rp/\varepsilon)^4]}$] (in atomic units) where $\alpha = 1$ and $\varepsilon = 1$ (a) and $\alpha = 1$ and $\varepsilon = 2$ (b) show that for $rp \ll \varepsilon$, the potential becomes very repulsive. Since V^H and V^P have similar functional forms, common notations are used to denote the potentials and their corresponding variables: $V(r, p)$ denotes V^H or V^P , α denotes α_H or α_P , ε denotes ε_H or ε_P , r denotes r_i or r_{ij} , and p denotes p_i or p_{ij} . Therefore, the highly repulsive behavior of $V(r, p)$ as $rp \ll \varepsilon$ enforces the Heisenberg and Pauli principles within the classical framework.

Similar steps lead to $\{\sum_{i=1}^N L_{iy}, H\} = 0$ and $\{\sum_{i=1}^N L_{iz}, H\} = 0$, resulting in

$$\frac{d\mathbf{L}_T}{dt} = \{\mathbf{L}_T, H\} = 0. \quad (13)$$

Therefore, the total angular momentum is also a conserved quantity for a Hamiltonian with MDPs that are spherically symmetric in position and momentum space.

III. GROUND STATE ENERGIES

In the next four sections we will examine ground state, excited state, ionization, and scattering properties of MDPs, beginning in this section with ground-state energies. This requires the choice of a specific MDP, and we have chosen the KW MDP because ground states of many-electron atoms have been modeled with KW MDP [57] (therefore, we drop the KW designation in what follows). Before we continue it is important to specify more precisely the strategy. The empirical parameters in this model are used to train the model to match Hartree-Fock (HF) ground-state energies of a subset of the elements [77]. The trained model is then tested for its transferability to ionization energies and ground-state energies of other elements that were not used in the training.

The MDP interaction between an electron and the nucleus is stabilized by the Heisenberg MDP

$$V^H(r_i, p_i) = \frac{\varepsilon_H^2 \hbar^2}{4\alpha_H m_e r_i^2} e^{\alpha_H[1-(r_i p_i/\varepsilon_H \hbar)^4]}, \quad (14)$$

where m_e is mass of electron, r_i and p_i are the magnitudes of position and momentum of the i th electron relative to the nucleus, and ε_H and α_H are parameters. Because V^H is

more repulsive, scaling as r^{-2} , than the attractive electron-ion attraction, scaling as $-r^{-1}$, the electron resides in a potential at a finite distance from the nucleus. The ion is taken to be at rest relative to the electron due to the large ion-electron mass ratio. However, the KW prescription only includes a Heisenberg interaction between species and no statistical interaction between ions by its definition [78]. For a many-electron atom, the Pauli exclusion principle is incorporated through the Pauli MDP expressed as

$$V^P(r_{ij}, p_{ij}) = \frac{\varepsilon_P^2 \hbar^2}{4\alpha_P m_e r_{ij}^2} e^{\alpha_P[1-(r_{ij} p_{ij}/\varepsilon_P \hbar)^4]}, \quad (15)$$

where r_{ij} and p_{ij} are the magnitudes of relative position and momentum of the i th and j th electron, respectively, and ε_P and α_P are parameters. V^H tries to impose the condition $r_i p_i \geq \varepsilon_H \hbar$, which is analogous to the Heisenberg uncertainty principle, and V^P tries to impose the condition $r_{ij} p_{ij} \geq \varepsilon_P \hbar$, which is analogous to the Pauli exclusion principle. The region excluded from phase space by Pauli and Heisenberg MDPs is referred to as the ‘‘core.’’ ε_H and ε_P are parameters that decide the size of the core, while α_H and α_P are parameters that decide the hardness of exclusion from the core. Note that V^H and V^P have similar functional forms. Therefore, they are illustrated in a combined manner as $r^2 V(r, p)$ in Fig. 1, where V denotes V^H or V^P , r denotes r_i or r_{ij} , and p denotes p_i or p_{ij} . From Fig. 1 we can infer that for $r_i p_i \ll \varepsilon_H \hbar$ and $r_{ij} p_{ij} \ll \varepsilon_P \hbar$ the potentials become very repulsive, thereby enforcing the Heisenberg and Pauli principles within the classical framework. The properties of the ground state depend on the values of the core sizes and the hardness parameters. For simplicity [79], we try to quantify the influence of core sizes

on the ground-state energies; therefore, we fix the values of the hardness parameters α_H and α_P to be 2 and 1, respectively, as suggested by Beck *et al.* [80] based on their stopping power studies.

The ground state of a many-electron atom is obtained by minimization of the Hamiltonian with respect to positions and momenta of the electrons keeping their spins fixed, which requires a simultaneous solution for the set of equations $\frac{\partial H}{\partial \mathbf{r}_i} = 0$ and $\frac{\partial H}{\partial \mathbf{p}_i} = 0$ for $i = 1$ to N_e . The minimized Hamiltonian would result in a frozen configuration for the ground state with zero electron velocities but nonzero momenta, as mentioned below Eq. (5). Thus, the MDP model has the desired nonclassical behavior. The energy of the minimized Hamiltonian gives the ground-state energy E . The electrons are assigned successive spin values of $1/2$ and $-1/2$ and are initialized with certain position and momentum values prior to minimization. Atomic units were used for the calculation. Following Ref. [57], minimization was performed using the Broyden-Fletcher-Goldfarb-Shanno (BFGS) algorithm [81] as implemented in the MATLAB solver “fminunc.” BFGS is an unconstrained optimization method belonging to the class of quasi-Newton methods. Despite the use of BFGS we cannot be sure that the optimization results in a global minimum. To identify the core sizes that resulted in ground-state energies in close agreement with HF (Hartree-Fock) values we performed the minimization for a range of core sizes for some elements. For an atom with M electrons, the Hamiltonian is a function of $6M$ variables; therefore, the cost of minimization increases as M becomes larger. On a laptop with Intel Core i3 processor (2.53 GHz and 4 GB RAM) it took about 4 sec and 5 min to obtain the ground states of nitrogen and calcium, respectively. A search in the parameter space requires a number of minimizations, therefore, we performed the search only for

some elements, namely, nitrogen (N), neon (Ne), aluminum (Al), argon (Ar), and calcium (Ca).

Correlated core sizes ($\varepsilon_H, \varepsilon_P$)

The percentage deviation from HF defined as $\Delta_{HF}(\alpha_H, \alpha_P) = 100|(E - E_{HF})/E_{HF}|$ was traced as a surface for N, Ne, Al, Ar, and Ca for ε_H spanning from about 1 to 2 and ε_P spanning from about 1 to 2.5. The space was discretized with a grid spacing of 0.01, therefore about 15 000 minimizations were performed for each element considered. After parallelizing, minimizations to trace the surface for Ca on a node with about 10 cores took about 2 days. The search was crucial because the search led us to identify correlated ε_H and ε_P values that resulted in ground-state energies in very good agreement with HF values for all the elements considered. Figure 2 shows the projected surface of Δ_{HF} for Al and Ca and the correlated ($\varepsilon_H, \varepsilon_P$) points that correspond to $\Delta_{HF} \lesssim 4\%$. Using the same condition, the correlated set of ($\varepsilon_H, \varepsilon_P$) were extracted from Δ_{HF} surfaces of other elements considered (N, Ne, and Ar) as shown in Fig. 3(b) (points). Relative error with respect to HF values $\Delta_{HF}(\%)$, are shown in Fig. 3(a). For each of these elements the ground-state energy with minimum Δ_{HF} are comparable with ground-state energy experimentally measured [82].

We observed that the correlated ($\varepsilon_H, \varepsilon_P$) follow a pattern with respect to atomic number (Z), that is, the correlation extends to higher values of ε_H with increasing atomic number, as seen in Fig. 3(b). The reason for this pattern is not understood. The correlation between ε_H and ε_P is captured well by a parabolic relation expressed as

$$\varepsilon_P = A(Z)\varepsilon_H^2 + B(Z)\varepsilon_H + C(Z). \quad (16)$$

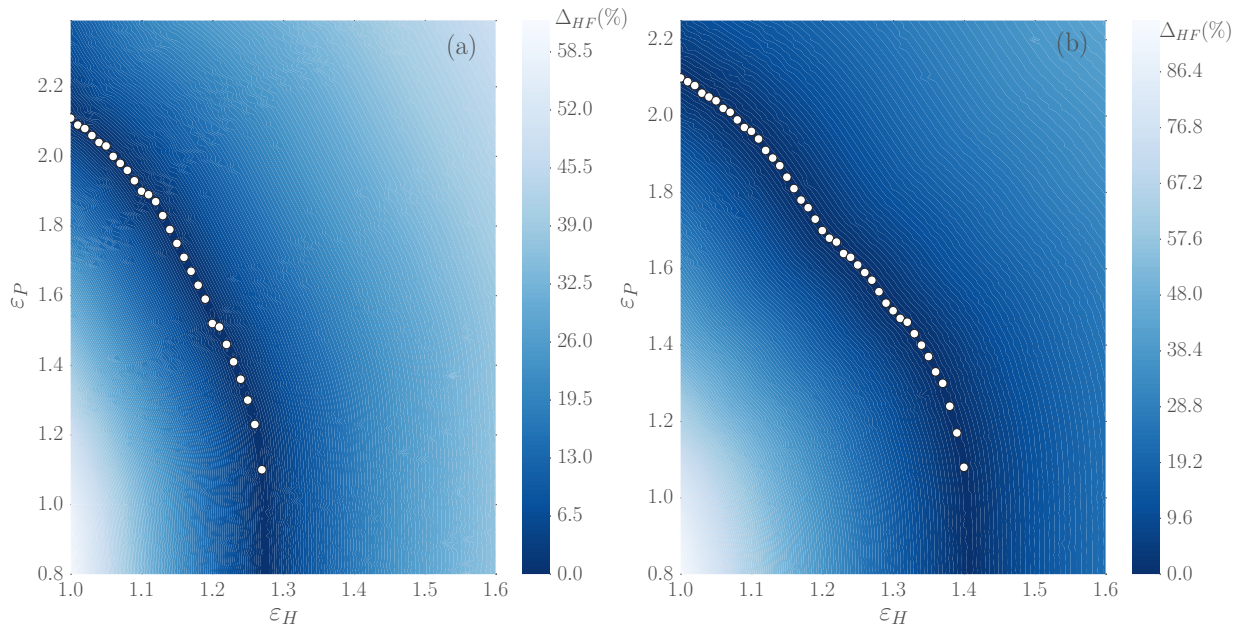


FIG. 2. Projected surface of $\Delta_{HF}(\%) = 100|(E - E_{HF})/E_{HF}|$ in $(\varepsilon_H, \varepsilon_P)$ plane for Al (a) and Ca (b) showing the region of minima. $(\varepsilon_H, \varepsilon_P)$ points (white dots) corresponding to $\Delta_{HF} \lesssim 4\%$ follow a curve indicating that there is a correlation between ε_H and ε_P values that result in ground-state energies which are in very good agreement with HF values. The correlation between the parameters reveal some degree of transferability to ground-state energies of other elements that are not tested.

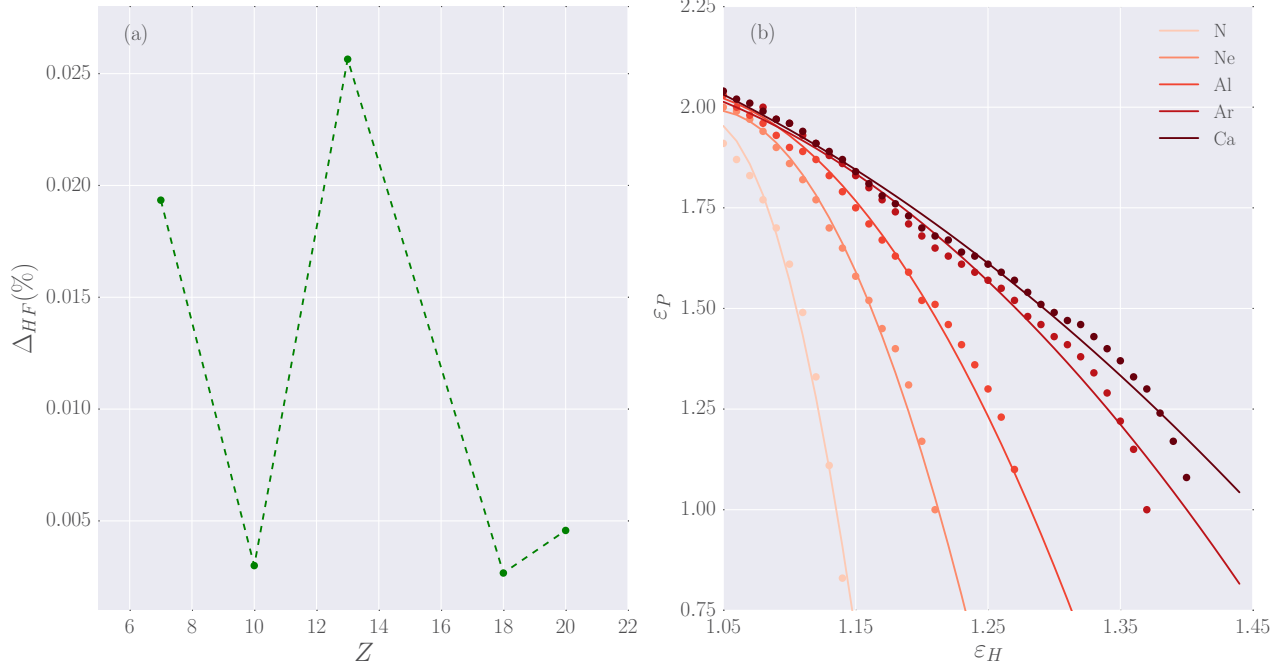


FIG. 3. (a) Relative error Δ_{HF} (%) of MDP prediction of ground-state energies with respect to HF values (green circles connected by dashed green line) for N, Ne, Al, Ar, and Ca show that the KW formulation is an excellent model for ground-state energies (lines are to guide the eye). (b) Correlated $(\varepsilon_H, \varepsilon_P)$ points (circles in shades of red from light to dark corresponding to increasing atomic number) extracted from the Δ_{HF} surfaces. Also shown are curve fits (solid curves in shades of red increasing from light to dark corresponding to increasing atomic number) using $\varepsilon_P = A\varepsilon_H^2 + B\varepsilon_H + C$ for N, Ne, Al, Ar, and Ca. For all the elements considered, the curve fits match well with the points extracted from the corresponding Δ_{HF} surfaces, suggesting a possible transferability with respect to the atomic number.

There is no particular reason for expressing ε_P as a function of ε_H ; a similar fit would yield ε_H as a function of ε_P . We quantified the pattern with respect to atomic number by fitting the coefficients A, B , and C to fourth degree polynomials as shown in Fig. 4(a). We then interpolated the coefficients for fluorine (F) and sulfur (S) to obtain their correlated $(\varepsilon_H, \varepsilon_P)$ that resulted in ground-state energies in good agreement with HF. The maximum Δ_{HF} was $\sim 10\%$ and $\sim 5\%$ for F and S, respectively. This is remarkable because it confirms the transferability of the trained $(\varepsilon_H, \varepsilon_P)$ to ground-state energies of F and S that were not included in the training. Figure 4(b) shows the interpolated $(\varepsilon_H, \varepsilon_P)$ curves of F and S along with the parabolic fits of $(\varepsilon_H, \varepsilon_P)$ for N, Ne, Al, Ar, and Ca.

IV. EXCITED STATE ORBITS

In this section we turn to excited state properties, defined as $\dot{\mathbf{r}} \neq 0, \dot{\mathbf{p}} \neq 0$, and $H < 0$. Again, we make use of the MDP, but for an electron-ion pair with the simpler Hamilton equations given by

$$\begin{aligned} \frac{d\mathbf{r}}{dt} &= \frac{\mathbf{p}}{m_e} + \frac{\partial V_{\text{eff}}(r, p)}{\partial \mathbf{p}}, \\ \frac{d\mathbf{p}}{dt} &= -\frac{\partial V_{\text{eff}}(r, p)}{\partial \mathbf{r}}, \end{aligned} \quad (17)$$

where $V_{\text{eff}}(r, p)$ contains both the attractive Coulomb potential and the (repulsive) Heisenberg MDP.

In contrast with the minimization procedure used in the previous section, we now examine several initial value prob-

lems for (17). The Hamilton equations (17) with ionic charge $Z = 1, \alpha_H = 5$, and $\varepsilon_H = 0.9535$ were numerically integrated (after conversion to atomic units) using MATLAB's RK45 integrator. We considered the following initial conditions: (i) $\mathbf{r} = 1\hat{\mathbf{x}}, \mathbf{p} = 1\hat{\mathbf{y}}$, (ii) $\mathbf{r} = 1\hat{\mathbf{x}}, \mathbf{p} = \frac{1}{\sqrt{2}}\hat{\mathbf{x}} + \frac{1}{\sqrt{2}}\hat{\mathbf{y}}$, (iii) $\mathbf{r} = 1\hat{\mathbf{x}}, \mathbf{p} = 1\hat{\mathbf{x}}$; these choices yield quite different behaviors. As shown in Fig. 5(a), the trajectory is Kepler-like (blue curve) for initial condition (i), is of zig-zag nature (green curve) for (ii), and is a reciprocating pattern (red curve) for (iii). Note that condition (iii) corresponds to zero initial angular momentum, which is an important test of any MDP; zero initial angular momentum would result in a Coulomb catastrophe in the absence of the proper MDP. The stabilizing nature is due to the dominant $1/r^2$ contribution in the MDP in the limit of $p = 0$ or $rp = \varepsilon_H$, compared to the (infinitely deep) attractive Coulomb potential $-1/r$. We found the energy and angular momentum to be conserved for all three trajectories as expected from Sec. II.

One way of interpreting the trajectories' nature is by superimposing their (r, p) dynamics on the total energy contour as shown in Fig. 5(b). Depending on the initial condition, the electron executes a trajectory that confines its energy to a contour marked by its initial energy. This implies that the minimum of the confining potential $V_{\text{eff}}(r, p)$ changes with the electron's momentum in accordance with energy conservation. Further, though Fig. 5(b) gives the impression that (r, p) dynamics for the three different trajectories overlap with each other, Figs. 5(c) and 5(d) showing the magnified regions 1 and 2 of Fig. 5(b) reveal a kind of band structure in their (r, p) dynamics that do not exactly overlap with each other.

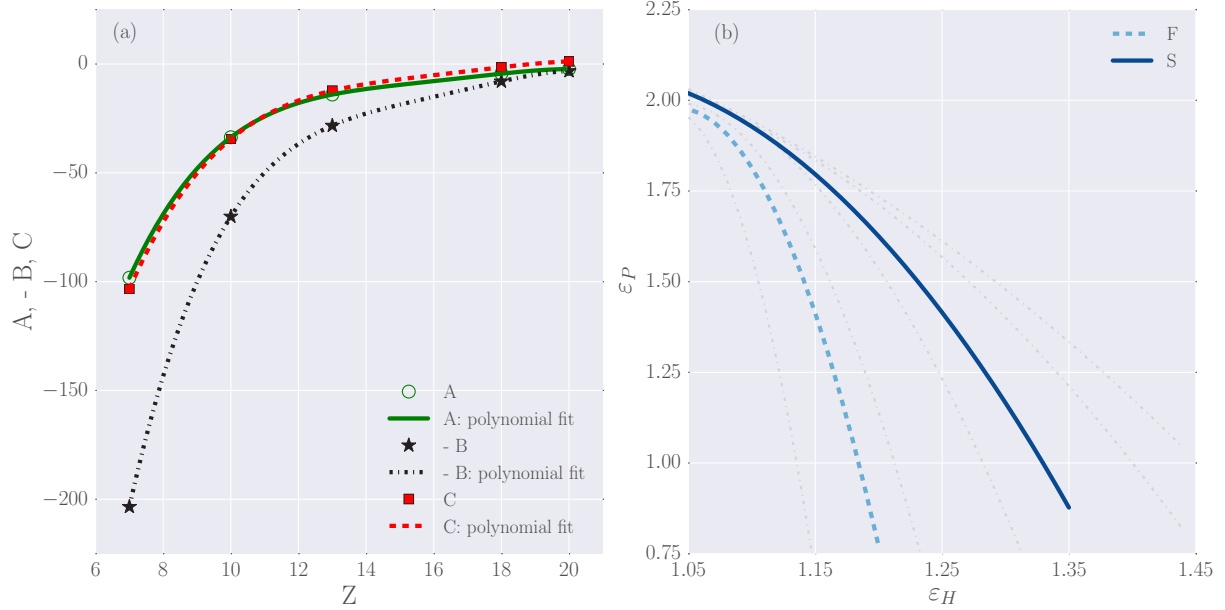


FIG. 4. (a) Coefficients A, B, and C of the fit $\varepsilon_P = A\varepsilon_H^2 + B\varepsilon_H + C$ vary as a function of atomic number (Z). The pattern in the data points of A (green circles), B (black star), and C (red squares) corresponding to N, Ne, Al, Ar, and Ca are captured well by fourth degree polynomial fits for A (solid green curve), B (dotted black curve), and C (dashed red curve). (b) Correlated $(\varepsilon_H, \varepsilon_P)$ curves for F (blue dashed) and S (blue solid) computed with A, B, and C interpolated using their corresponding fourth degree polynomial fits. Ground state energies for F and S from their correlated $(\varepsilon_H, \varepsilon_P)$ are in good agreement with HF values (with a maximum Δ_{HF} of $\sim 10\%$ and $\sim 5\%$ for F and S, respectively). This confirms the transferability of the trained $(\varepsilon_H, \varepsilon_P)$ to ground-state energies of elements that were not included in the training.

V. FIRST AND SECOND IONIZATION ENERGIES

The identity (being bound or free) of an electron in a finite-temperature plasma is continuously changing. Moreover, in processes such as charged-particle stopping, much of the energy loss can be due to ionization [83]. Therefore, in addition to atomic properties, MDPs must accurately capture transitions between bound and free states. In this subsection we examine these properties through comparisons of predicted first and second ionization energies with experimental values. We do this in a manner that allows us to assess the transferable properties of the MDPs by using parameters previously trained on ground-state properties.

The n th ionization energy is given by

$$I_n = E_n - E_0, \quad (18)$$

where E_n is the energy of an ion with n electrons removed and E_0 is the (ground-state) energy of the neutral atom. E_n for $n = 1, 2$ were obtained by minimizing the corresponding Hamiltonian using the same minimization algorithm employed above for every correlated ε_H and ε_P pair trained on the ground-state energy of the corresponding neutral atom. The corresponding set of first and second ionization energies were then computed. From this set, we chose those that minimized the combined error defined as

$$\Delta E_{GS,1,2} = (E_{GS} - E_{HF})^2 + (I_1 - I_{1,\text{expt.}})^2 + (I_2 - I_{2,\text{expt.}})^2, \quad (19)$$

where $I_{1,\text{expt.}}$ and $I_{2,\text{expt.}}$ are experimentally measured first and second ionization energies given by NIST data [82]. As shown in Fig. 6, first ionization energies are in good agreement with the NIST data, while the second ionization energies yield

mixed results. Therefore, the parameters ε_H and ε_P trained to give very accurate neutral ground-state energies transfer well to the prediction of first and second ionization energies, with some outliers.

VI. SCATTERING PROPERTIES OF FREE ELECTRON STATES

In this section we examine our fourth criteria for plasma behavior: scattering properties of continuum states. We quantify the MDP's ability to accurately describe continuum properties through tests based on the momentum transfer cross section (MTCS), an important quantity related to stopping power [84–86] and other transport properties [87]. As in previous sections, we reduce the many-body Hamiltonian to a simpler system of an electron scattered by a screened ion. The Hamiltonian in the reference frame of the ion is given by

$$H_C = \frac{p^2}{2m_e} + V^Y(r), \quad (20)$$

$$V^Y(r) = -\frac{Ze^2}{r} e^{-r/\lambda}, \quad (21)$$

where Z is the ionic charge and λ is the screening length, which is chosen appropriate to a plasma; for example, for dense plasmas, λ is typically a finite temperature Thomas-Fermi screening length [88]. For the rest of this section atomic units have been used and λ is expressed through an inverse screening parameter $\kappa_B = a_B/\lambda$ where a_B is the Bohr radius.

We begin by comparing the quantum and classical MTCS to identify the conditions where they differ appreciably. The

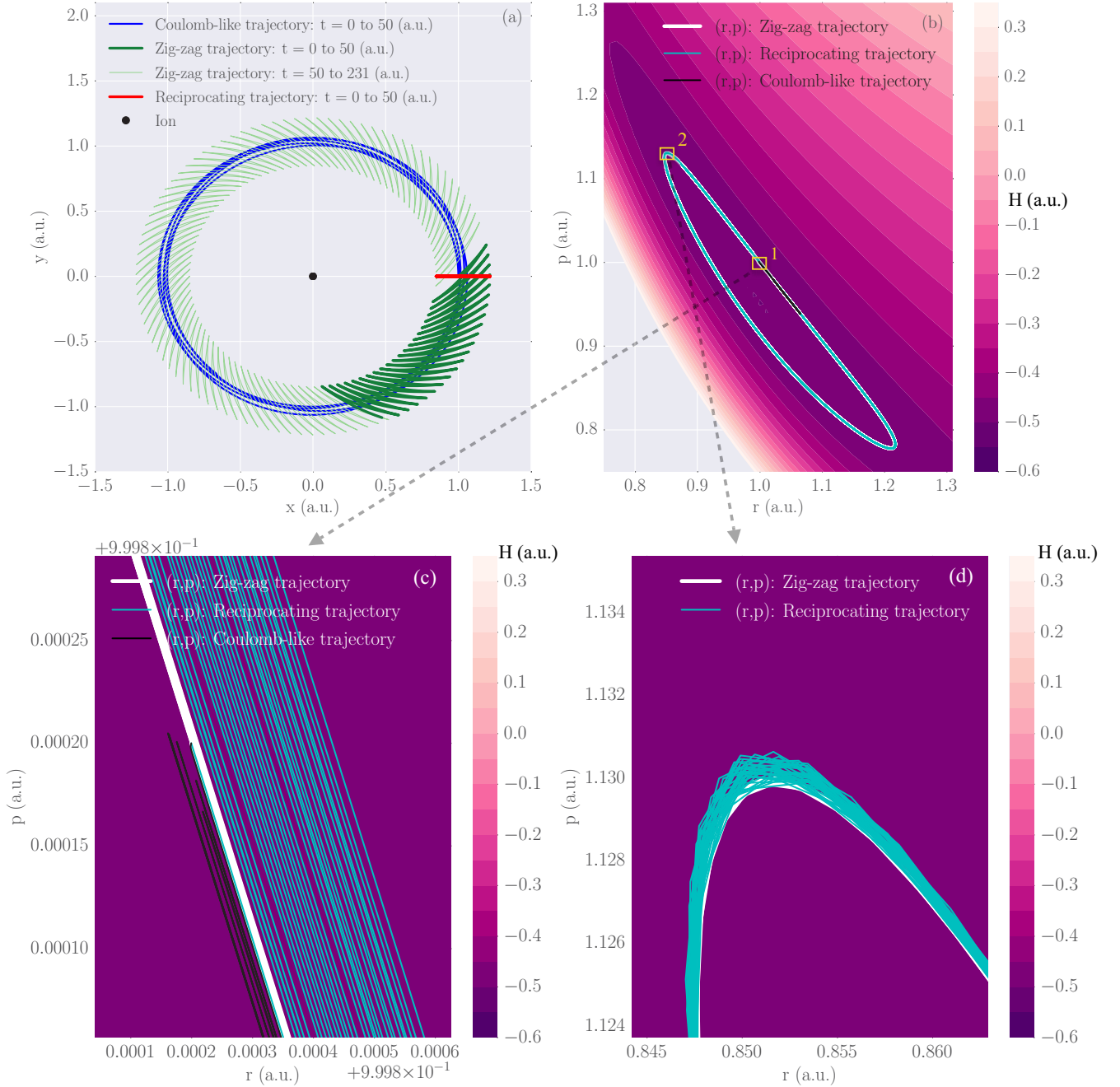


FIG. 5. (a) Electron trajectory around ion (black dot) corresponding to different initial conditions: Kepler-like motion from $t = 0$ to $t = 50$ a.u. (blue curve), zig-zag motion from $t = 0$ to $t = 50$ a.u. (dark green curve), zig-zag motion from $t = 50$ to $t = 231$ a.u. (light green curve), and reciprocating motion from $t = 0$ to $t = 50$ a.u. (red curve). Reciprocating motion corresponds to zero initial angular momentum, which would result in an unstable trajectory in the absence of Heisenberg MDP. (b) Magnitude of position (r) and magnitude of momentum (p) corresponding to the trajectories in (a) from $t = 0$ to $t = 50$ a.u. are superimposed on the Hamiltonian surface. (c) Region 1 of (b) magnified to show the bandlike structure in (r, p) dynamics. (d) Region 2 of (b) magnified to show a similar bandlike structure in (r, p) dynamics.

quantum MTCS is given by

$$\sigma_{tr}^{QM} = \frac{4\pi}{k^2} \sum_{l=0}^{\infty} (l+1) \sin^2(\delta_l - \delta_{l+1}), \quad (22)$$

where k is the magnitude of the wave vector of a free electron and δ_l is the phase shift for angular momentum quantum number l . For simplicity, we chose the WKB approximation

for δ_l [84,87], which is given by

$$\delta_l = \int dr \sqrt{k^2 - \frac{(l+1/2)^2}{r^2} - 2V^Y(r)} - \int dr \sqrt{k^2 - \frac{(l+1/2)^2}{r^2}}. \quad (23)$$

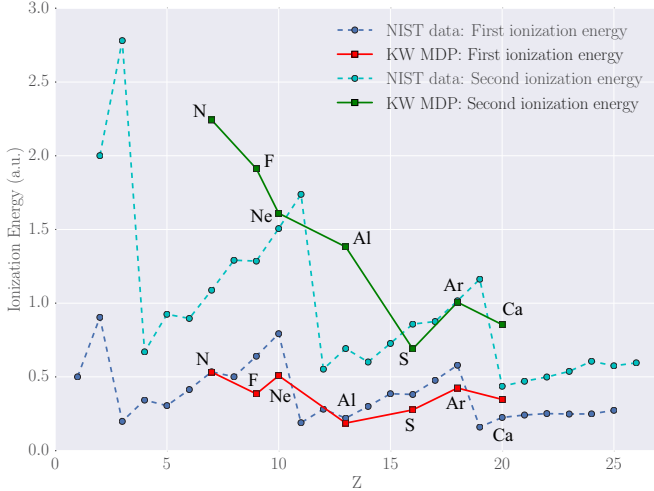


FIG. 6. For N, F, Ne, Al, S, Ar, and Ca, first and second ionization energies were computed using MDPs with the correlated $(\varepsilon_H, \varepsilon_P)$ optimized to give accurate neutral ground-state energies. MDP prediction of first ionization energies (red curve) is in good agreement with NIST data (dashed blue curve); second ionization energies using MDPs (green curve) yield mixed results compared to NIST data (dashed cyan curve). Therefore, the parameters trained on neutral ground-state energies transfer fairly well to the prediction of first and second ionization energies with some outliers.

The classical MTCS [87] is given by

$$\sigma_{tr}^{CL} = \int_0^\infty db [1 - \cos \theta(b)] b, \quad (24)$$

where $\theta(b)$ is the scattering angle for an impact parameter b . For a Hamiltonian without an MDP the scattering angle is given by the semianalytic formula

$$\theta(b) = \pi - 2b \int_{r_m}^\infty \frac{dr}{r^2} \frac{1}{\sqrt{1 - b^2/r^2 - V^Y(r)/E}}, \quad (25)$$

where r_m is the classical turning point given by the largest root of the equation

$$1 - \frac{b^2}{r_m^2} - \frac{V^Y(r_m)}{E} = 0. \quad (26)$$

Now, for a Hamiltonian with an MDP, Eq. (25) cannot be applied; therefore, we computed the scattering angle from the electron's trajectory, which was obtained by numerically integrating its Hamilton equations until the electron-ion interaction became negligible. We refer to this as the trajectory method for MTCS. For the purely classical case with $Z = 1$, $\kappa_B = 1$, and energy range $E = 10$ to 100 a.u., we compared the MTCS from trajectories with the semianalytic MTCS Eq. (25). They are in good agreement as shown in Fig. 7, thereby validating our implementation. For the same conditions, the quantum MTCS differ appreciably from the classical MTCS as shown in Fig. 7. Also shown in Fig. 7 are asymptotic limits of the classical and quantum MTCS values (denoted by $\sigma_{tr,asym}^{CM}$ and $\sigma_{tr,asym}^{QM}$ respectively) derived in Ref. [89] that have analytic expressions

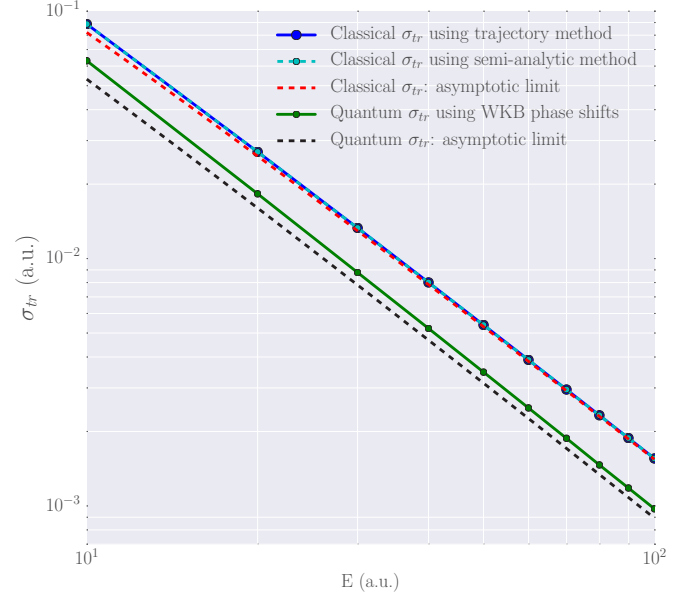


FIG. 7. Comparison of the classical and quantum MTCS for $Z = 1, \kappa_B = 1$, and $E = 10$ to 100 a.u. The classical MTCS using semianalytic method (blue dashed) and the trajectory method (cyan dashed) are in very good agreement. They also match with the asymptotic limit of the classical MTCS (red dashed) given by Eq. (27). The quantum MTCS (black dashed) differ significantly from the classical result. Also shown is the asymptotic limit of the quantum MTCS (pink dashed) given by Eq. (28) with the difference from the numerical quantum MTCS decreasing as energy increases.

given by

$$\sigma_{tr,asym}^{CM} = 4\pi \left(\frac{Z}{2E} \right)^2 \left[\ln \left(\frac{4E}{Z} \lambda \right) - \gamma - \frac{1}{2} \right], \quad (27)$$

$$\sigma_{tr,asym}^{QM} = 4\pi \left(\frac{Z}{2E} \right)^2 \left[\ln(2\sqrt{2E}\lambda) - \frac{1}{2} \right], \quad (28)$$

where $\gamma = 0.577$ [89]. These expressions reveal that in the asymptotic limit, the quantum MTCS qualitatively differs from the classical MTCS due to a lower limit set by the deBroglie wavelength on the distance of closest approach for quantum scattering. Therefore, the test for MDP is if it can include the necessary quantum effects to bridge the gap between classical and quantum MTCS values.

Since the interaction is between an electron and a screened ion, Heisenberg MDP is added to H_C [Eq. (20)]. Using the trajectory method, we computed scattering angles for a range of impact parameters for $\alpha_H = 1$ and $\varepsilon_H = 0.125, 0.25$, and 0.5, as shown in Fig. 8. We found a structure in the scattering angles for low-impact parameters which is due to the MDP's influence on the electron-ion interaction as evident in the electron trajectories for $b = 0.026, 0.028$, and 0.03, as shown in Fig. 9(b). Those trajectories correspond to the impact parameter range where the scattering angle decreases to zero and then increases [as marked by the vertical dotted lines in Fig. 9(a)]. We performed an optimization with respect to the free parameters, α_H and ε_H , to minimize the squared difference between the quantum MTCS and the MTCS using MDP. The

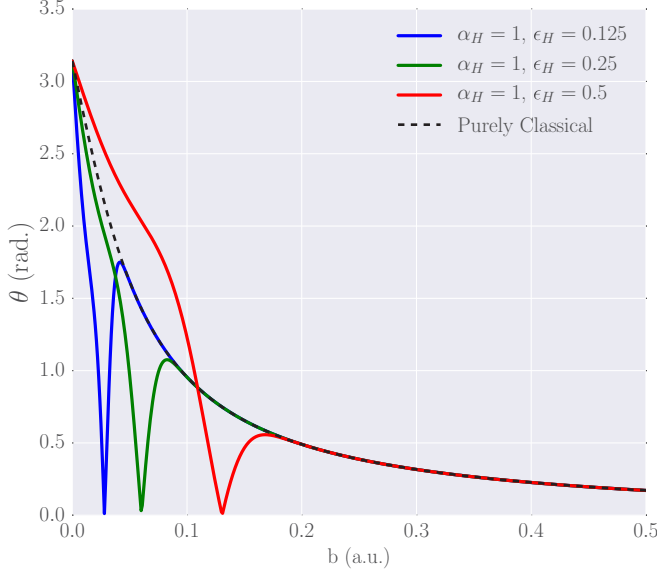


FIG. 8. Scattering angle θ vs impact parameter b corresponding to $Z = 1, \kappa_B = 1$, and $E = 10$ a.u. for the purely classical case (black dashed curve) and with Heisenberg MDP (blue curve: $\alpha_H = 1, \epsilon_H = 0.125$; green curve: $\alpha_H = 1, \epsilon_H = 0.25$; red curve: $\alpha_H = 1, \epsilon_H = 0.5$). Scattering at low impact parameters is highly influenced by the MDP, resulting in a structure in the scattering angles with the angle decreasing to zero and then increasing as impact parameter increases. Scattering angles of all the curves overlap with each other for large impact parameters.

optimized MTCS using MDP are close to the purely classical values, as shown in Fig. 10(a), implying that the MDP doesn't

incorporate the required quantum effects despite having a strong effect on the electron-ion scattering for small impact parameters. Figure 10(b) shows the filled contour of MTCS for a range of α_H and ϵ_H for $Z = 1, \kappa_B = 1$, and $E = 25$ a.u. The lowest MTCS value on the MTCS contour is about 0.016 a.u. which is larger than the corresponding quantum MTCS value of 0.0122 a.u. Similar observations were made from MTCS contours for energies in the range of 10 to 100 a.u. for $Z = 1$ and $\kappa_B = 1$. Therefore, though MDP serves as a good model for ground-state energies and first ionization energies of many-electron atoms, it is unable to incorporate the quantum effects in scattering of a free electron by a stationary screened ion, suggesting its limitation for plasmas.

VII. SUMMARY AND CONCLUSION

In summary, we have examined a time-dependent, quantum-mechanical method for large-scale simulations of nonequilibrium systems as an alternative to more expensive methods such as TD-DFT, TD-HF etc., and which relaxes most limitations associated with the relatively fast WPMD [47] and QSP [51] methods. In particular, our focus has been on the use of a classical-like, Hamiltonian-based framework based on effective momentum-dependent interactions [62] that has desirable conservation properties and the computational scaling of standard classical molecular dynamics. For simplicity, we employed the KW MDP form [62] since they have been quite successful for many atomic properties [58,61,66–70,72,73,75,76]. We examined their strengths and weaknesses for use in nonequilibrium dense plasma simulations using four criteria.

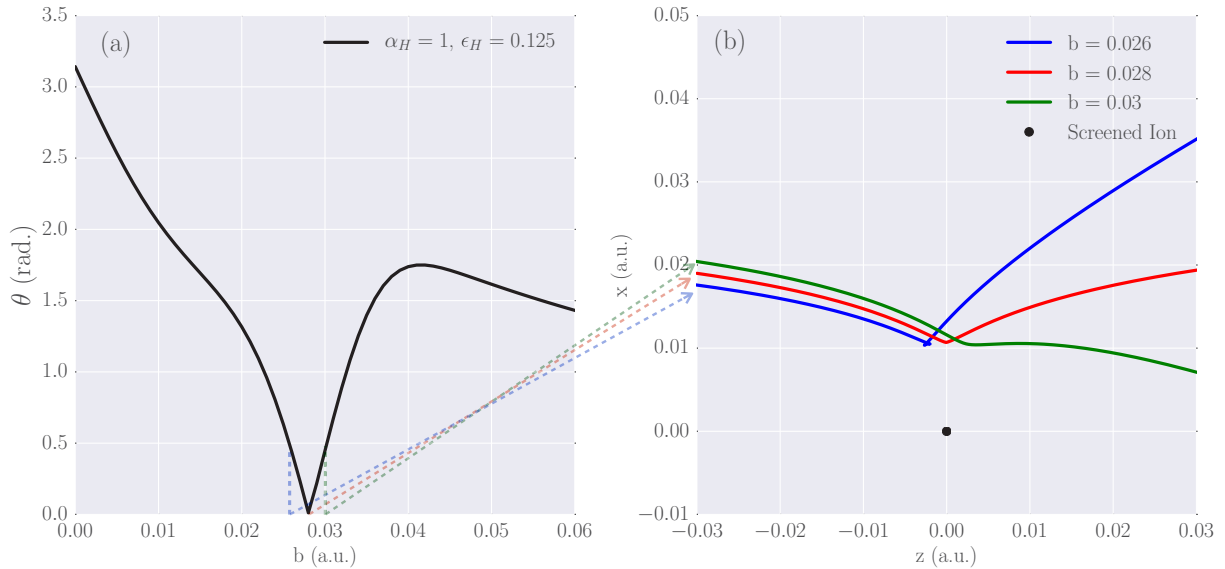


FIG. 9. (a) Scattering angle vs impact parameter obtained using MDP with $\alpha_H = 1, \epsilon_H = 0.125$ for $Z = 1, \kappa_B = 1$, and $E = 10$ a.u. There is a structure in the scattering angles with the angles becoming nearly zero for an impact parameter of $b = 0.028$ a.u. (b) Electron trajectory for $b = 0.028$ a.u. (red curve) reveals that though there is a strong interaction between the electron and the screened ion (black dot), the interaction is such that the scattering angle is nearly zero in the asymptotic limit of the trajectory. Electron trajectories for $b = 0.026$ a.u. (blue curve) and $b = 0.03$ a.u. (green curve) indicated by the vertical lines in (a) show that though the corresponding scattering angles are similar in magnitude, the nature of the trajectories are different with the electron scattered upward for $b = 0.026$ a.u. while the electron is scattered downward for $b = 0.03$ a.u.

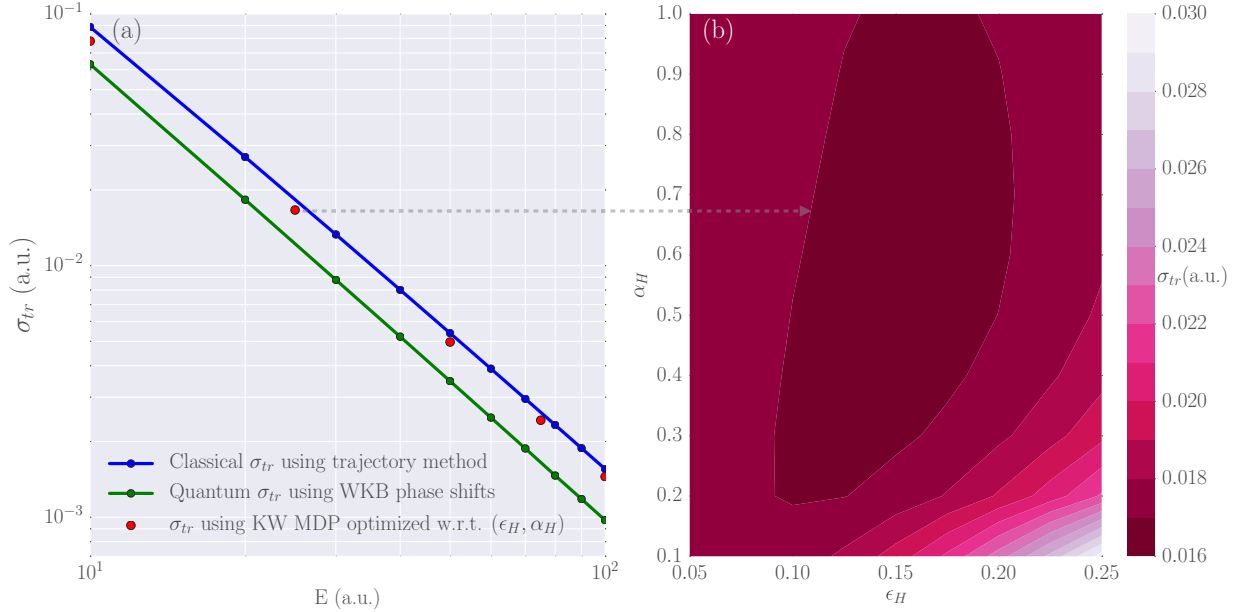


FIG. 10. (a) For $Z = 1$, $\kappa_B = 1$, and $E = 10$ to 100 a.u. the classical MTCS (blue curve) and the quantum MTCS (green curve) are compared with the MTCS using MDP (red dots) optimized with respect to its free parameters α_H and ϵ_H to minimize the squared difference between the quantum MTCS and the MTCS using MDP. (b) Filled contour of MTCS using MDP for a range of α_H and ϵ_H for $Z = 1$, $\kappa_B = 1$, and $E = 25$ a.u. The lowest value on the MTCS contour is 0.016 a.u., which is still large compared to the corresponding quantum MTCS value of 0.0122 a.u. Though the MDP significantly influences the electron-ion scattering for small impact parameters, its MTCS predictions are close to the classical MTCS suggesting the MDP's limitation for modeling electron-ion scattering in dense plasmas.

We first trained the parameters based on HF calculations to give accurate ground-state energies for neutral atoms with atomic number less than 20; the excellent agreement with HF calculations is shown in Fig. 3(a). We found a correlation between the parameters and fitted the correlation to a parabolic relation as shown in Fig. 3(b), revealing a level of transferability of these parameters to previously untrained systems.

Next, we computed the properties of excited state orbits of electron-ion pair and found disparate properties of the trajectories depending on the initial angular momentum, including unusual reciprocating patterns. An important feature of the KW MDP is the stabilization of the Coulomb catastrophe for the special case of zero initial angular momentum [see reciprocating motion case in Fig. 5(a)].

Because plasma electrons persistently undergo ionization and recombination events, we then turned to the ionization process itself, with the ionization energy as our quality metric for the MDP. From the fixed, previously determined ground-state parameters we predicted the first- and second-ionization energies and found first ionization ionization energies to be in good agreement with experimental values, again suggesting good transferability. However, the second ionization energies were mixed, with half accurate and half with an error as large as a factor of two, as shown in Fig. 6. The reason for this behavior in the second ionization energy is currently unknown.

Finally, we examined continuum states responsible for electronic transport processes, such as stopping power [84] and electrical and thermal conductivity [87]. We chose to examine the ability of the KW MDP to reproduce the MTCS versus energy for electron-ion collisions. A screened interaction was

chosen because it more realistically represents the dense plasma environment and because the Rutherford MTCS has pathological properties (i.e., a large impact parameter divergence) in this context. Using a WKB approach [87], we computed the classical and quantum MTCS and compared with predictions from KW MDP trajectories. As we showed in Fig. 10, KW MDP cannot yield the correct MTCS *despite training the parameters*, suggesting that the functional form itself is responsible. Thus, although KW MDPs were successful for ground-state properties, they cannot capture scattering properties important for plasma simulations.

The results presented here were for isolated atoms and ions. To quantify the implications of our findings on many-body properties of a plasma, large-scale molecular dynamics simulations are needed; this is beyond the scope of the present work and will be explored in a future work. However, our results have suggested several areas of improvement. First, the KW forms did not include a Heisenberg interaction between electrons, which is unphysical. Second, the functional form of the KW appears to have emerged to recover a Bohr picture of the ground state, which yields poor properties for scattering states. Third, alternate training methods should be explored, including optimizing on several properties (e.g., ground-state energy and cross sections) simultaneously. Such explorations are underway and will be the subject of a future work.

ACKNOWLEDGMENT

The work was supported by the Air Force Office of Scientific Research.

- [1] J. A. Frenje, P. E. Grabowski, C. K. Li, F. H. Séguin, A. B. Zylstra, M. Gatu Johnson, R. D. Petrasso, V. Y. Glebov, and T. C. Sangster, Measurements of Ion Stopping Around the Bragg Peak in High-Energy-Density Plasmas, *Phys. Rev. Lett.* **115**, 205001 (2015).
- [2] A. B. Zylstra *et al.*, Development of a WDM platform for charged-particle stopping experiments, *J. Phys.: Conf. Series* **717**, 012118 (2016).
- [3] W. Bang *et al.*, Visualization of expanding warm dense gold and diamond heated rapidly by laser-generated ion beams, *Sci. Rep.* **5**, 14318 (2015).
- [4] W. Bang *et al.*, Linear dependence of surface expansion speed on initial plasma temperature in warm dense matter, *Sci. Rep.* **6**, 29441 (2016).
- [5] D. A. Chapman and D. O. Gericke, Analysis of Thomson Scattering from Nonequilibrium Plasmas, *Phys. Rev. Lett.* **107**, 165004 (2011).
- [6] P. M. Kozłowski *et al.*, Theory of Thomson scattering in inhomogeneous media, *Sci. Rep.* **6**, 24283 (2016).
- [7] D. S. Rackstraw, O. Ciricosta, S. M. Vinko, B. Barbrel, T. Burian, J. Chalupský, B. I. Cho, H.-K. Chung, G. L. Dakovski, K. Engelhorn, V. Hájková, P. Heimann, M. Holmes, L. Juha, J. Krzywinski, R. W. Lee, S. Toleikis, J. J. Turner, U. Zastra, and J. S. Wark, Saturable Absorption of an X-Ray Free-Electron-Laser Heated Solid-Density Aluminum Plasma, *Phys. Rev. Lett.* **114**, 015003 (2015).
- [8] S. M. Vinko *et al.*, Investigation of femtosecond collisional ionization rates in a solid-density aluminium plasma, *Nat. Commun.* **6**, 6397 (2015).
- [9] T. C. Killian, Ultracold neutral plasmas, *Science* **316**, 705 (2007).
- [10] M. D. Knudson, M. P. Desjarlais, and D. H. Dolan, Shock-wave exploration of the high-pressure phases of carbon, *Science* **322**, 1822 (2008).
- [11] K. R. Cochrane *et al.*, Magnetically launched flyer plate technique for probing electrical conductivity of compressed copper, *J. Appl. Phys.* **119**, 105902 (2016).
- [12] E. I. Moses *et al.*, The National Ignition Facility: Ushering in a new age for high energy density science, *Phys. Plasmas* **16**, 041006 (2009).
- [13] D. Kraus, D. A. Chapman, A. L. Kritcher, R. A. Baggott, B. Bachmann, G. W. Collins, S. H. Glenzer, J. A. Hawreliak, D. H. Kalantar, O. L. Landen, T. Ma, S. LePape, J. Nilsen, D. C. Swift, P. Neumayer, R. W. Falcone, D. O. Gericke, and T. Döppner, X-ray scattering measurements on imploding CH spheres at the National Ignition Facility, *Phys. Rev. E* **94**, 011202 (2016).
- [14] B. Nagler *et al.*, The matter in extreme conditions instrument at the Linac Coherent Light Source, *J. Synchrotron Radiat.* **22**, 520 (2015).
- [15] C. Bostedt *et al.*, Linac Coherent Light Source: The first five years, *Rev. Mod. Phys.* **88**, 015007 (2016).
- [16] K. Tiedtke *et al.*, The soft x-ray free-electron-laser FLASH at DESY: Beamlines, diagnostics and end-stations, *New J. Phys.* **11**, 023029 (2009).
- [17] E. Plönjes and K. Tiedtke, in *Optical Technologies for Extreme-Ultraviolet and Soft X-ray Coherent Sources*, edited by F. Canova and L. Poletto, Springer Series in Optical Sciences (Springer, Heidelberg, 2015), Chap. I, pp. 1–21.
- [18] E. J. Gamboa *et al.*, Imaging x-ray crystal spectrometer for laser-produced plasmas, *J. Instrum.* **6**, P04004 (2011).
- [19] E. J. Gamboa *et al.*, Imaging x-ray Thomson scattering spectrometer design and demonstration, *Rev. Sci. Instrum.* **83**, 10E108 (2012).
- [20] P. Maragakis *et al.*, Microsecond molecular dynamics simulation shows effect of slow loop dynamics on backbone amide order parameters of proteins, *J. Phys. Chem. B* **112**, 6155 (2008).
- [21] J. L. Klepeis *et al.*, Long-timescale molecular dynamics simulations of protein structure and function, *Curr. Opin. Struct. Biol.* **19**, 120 (2009).
- [22] D. E. Shaw *et al.*, Millisecond-scale molecular dynamics simulations on Anton, in *Proceedings of the Conference on High Performance Computing Networking, Storage and Analysis (SC09)* (ACM, New York, 2009).
- [23] W. Eckhardt *et al.*, 591 TFLOPS Multi-trillion particles simulation on SuperMUC, in *Proceedings of Supercomputing, 28th International Supercomputing Conference, ISC 2013, Leipzig, Germany, June 16–20, 2013*, edited by J. M. Kunkel, T. Ludwig, and H. W. Meuer, Lecture Notes in Computer Science, Vol. 7905 (Springer-Verlag, Berlin, Heidelberg, 2013).
- [24] M. H. Viet *et al.*, Picosecond infrared laser-induced all-atom nonequilibrium molecular dynamics simulation of dissociation of viruses, *Phys. Chem. Chem. Phys.* **18**, 11951 (2016).
- [25] J. R. Perilla *et al.*, All-Atom Molecular Dynamics of Virus Capsids as Drug Targets, *J. Phys. Chem. Lett.* **7**, 1836 (2016).
- [26] R. Car and M. Parrinello, Unified Approach for Molecular Dynamics and Density-Functional Theory, *Phys. Rev. Lett.* **55**, 2471 (1985).
- [27] G. Kresse and J. Hafner, *Ab initio* molecular dynamics for liquid metals, *Phys. Rev. B* **47**, 558(R) (1993).
- [28] T. G. White, S. Richardson, B. J. B. Crowley, L. K. Pattison, J. W. O. Harris, and G. Gregori, Orbital-Free Density-Functional Theory Simulations of the Dynamic Structure Factor of Warm Dense Aluminum, *Phys. Rev. Lett.* **111**, 175002 (2013).
- [29] M. Zhang and D. A. Drabold, An extension of the Kubo-Greenwood formula for use in molecular simulations, [arXiv:0904.0212](https://arxiv.org/abs/0904.0212) (2009).
- [30] Z. Chen, B. Holst, S. E. Kirkwood, V. Sametoglu, M. Reid, Y. Y. Tsui, V. Recoules, and A. Ng, Evolution of ac Conductivity in Nonequilibrium Warm Dense Gold, *Phys. Rev. Lett.* **110**, 135001 (2013).
- [31] P. A. M. Dirac, Note on exchange phenomena in the Thomas atom, *Math. Proc. Camb. Phil. Soc.* **26**, 376 (1930).
- [32] J. A. Maruhn *et al.*, The TDHF code Sky3D, *Comput. Phys. Commun.* **185**, 2195 (2014).
- [33] E. Runge and E. K. U. Gross, Density-Functional Theory for Time-Dependent Systems, *Phys. Rev. Lett.* **52**, 997 (1984).
- [34] S. Botti *et al.*, Time-dependent density-functional theory for extended systems, *Rep. Prog. Phys.* **70**, 357 (2007).
- [35] M. A. L. Marques *et al.*, *Fundamentals of Time-Dependent Density Functional Theory* (Springer, Heidelberg, 2012).
- [36] N. Ferré, M. Filatov, and M. Huix-Rotllant, *Density-Functional Methods for Excited States* (Springer, Heidelberg, 2016).
- [37] A. D. Baczewski, L. Shulenburg, M. P. Desjarlais, S. B. Hansen, and R. J. Magyar, X-ray Thomson Scattering in Warm Dense Matter Without the Chihara Decomposition, *Phys. Rev. Lett.* **116**, 115004 (2016).
- [38] X. Andrade *et al.*, Time-dependent density-functional theory in massively parallel computer architectures: The octopus project, *J. Phys. Condens. Matter* **24**, 233202 (2012).

- [39] N. A. Modine and R. M. Hatcher, Representing the thermal state in time-dependent density functional theory, *J. Chem. Phys.* **142**, 204111 (2015).
- [40] A. Pribram-Jones, P. E. Grabowski, and K. Burke, Thermal Density-Functional Theory: Time-Dependent Linear Response and Approximate Functionals from the Fluctuation-Dissipation Theorem, *Phys. Rev. Lett.* **116**, 233001 (2016).
- [41] R. W. Hockney and J. W. Eastwood, *Computer Simulation Using Particles* (CRC Press, New York, 1988).
- [42] K. Kadau *et al.*, Nanohydrodynamics simulations: An atomistic view of the RayleighTaylor instability, *Proc. Natl. Acad. Sci. U. S. A.* **101**, 5851 (2004).
- [43] P. E. Grabowski, M. P. Surh, D. F. Richards, F. R. Graziani, and M. S. Murillo, Molecular Dynamics Simulations of Classical Stopping Power, *Phys. Rev. Lett.* **111**, 215002 (2013).
- [44] Here we define “classical” as a computational method that involves a modest number of variables evolved in terms of ordinary differential equations; therefore, they allow the quantum problem to be mapped onto computational tools well-developed for classical systems. For example, Gaussian-based WPMD [47, 54, 55, 90] has eight ODEs per particle rather than the usual six. Similarly, MDPs have six degrees of freedom per particle, and the corresponding number of ODEs, but with extra force calculations.
- [45] F. Remacle and R. D. Levine, On the classical limit for electronic structure and dynamics in the orbital approximation, *J. Chem. Phys.* **113**, 4515 (2000).
- [46] D. V. Shalashilin and I. Burghardt, Gaussian-based techniques for quantum propagation from the time-dependent variational principle: Formulation in terms of trajectories of coupled classical and quantum variables, *J. Chem. Phys.* **129**, 084104 (2008).
- [47] P. E. Grabowski, A. Markmann, I. V. Morozov, I. A. Valuev, C. A. Fichtl, D. F. Richards, V. S. Batista, F. R. Graziani, and M. S. Murillo, Wave packet spreading and localization in electron-nuclear scattering, *Phys. Rev. E* **87**, 063104 (2013).
- [48] J. Schiff and B. Poirier, Communication: Quantum mechanics without wavefunctions, *J. Chem. Phys.* **136**, 031102 (2012).
- [49] B. Poirier, Bohmian mechanics without pilot waves, *Chem. Phys.* **370**, 4 (2010).
- [50] F. Lado, Effective potential description of the quantum ideal gases, *J. Chem. Phys.* **47**, 5369 (1967).
- [51] J. N. Glosli, F. R. Graziani, R. M. More, M. S. Murillo, F. H. Streitz, M. P. Surh, L. X. Benedict, S. Hau-Riege, A. B. Langdon, and R. A. London, Molecular dynamics simulations of temperature equilibration in dense hydrogen, *Phys. Rev. E* **78**, 025401(R) (2008).
- [52] C. S. Jones and M. S. Murillo, Analysis of semi-classical potentials for molecular dynamics and Monte Carlo simulations of warm dense matter, *High Energy Density Physics* **3**, 379 (2007).
- [53] T. Schlick and C. S. Peskin, Can classical equations simulate quantum-mechanical behavior? A molecular dynamics investigation of a diatomic molecule with a Morse potential, *Commun. Pure Appl. Math.* **42**, 1141 (1989).
- [54] H. Feldmeier and J. Schnack, Molecular dynamics for fermions, *Rev. Mod. Phys.* **72**, 655 (2000).
- [55] J. T. Su and W. A. Goddard III, Excited Electron Dynamics Modeling of Warm Dense Matter, *Phys. Rev. Lett.* **99**, 185003 (2007).
- [56] J. C. Snyder, M. Rupp, K. Hansen, K.-R. Müller, and K. Burke, Finding Density Functionals with Machine Learning, *Phys. Rev. Lett.* **108**, 253002 (2012).
- [57] J. S. Cohen, Quasiclassical effective Hamiltonian structure of atoms with $Z=1$ to 38, *Phys. Rev. A* **51**, 266 (1995).
- [58] Y. Zhou, C. Huang, Q. Liao, and P. Lu, Classical Simulations Including Electron Correlations for Sequential Double Ionization, *Phys. Rev. Lett.* **109**, 053004 (2012).
- [59] C. L. Kirschbaum and L. Wilets, Classical many-body model for atomic collisions incorporating the Heisenberg and Pauli principles, *Phys. Rev. A* **21**, 834 (1980).
- [60] J. S. Cohen, Extension of quasiclassical effective Hamiltonian structure of atoms through $Z=94$, *Phys. Rev. A* **57**, 4964 (1998).
- [61] J. S. Cohen, Molecular effects on antiproton capture by H_2 and the states of \overline{pp} formed, *Phys. Rev. A* **56**, 3583 (1997).
- [62] L. Wilets *et al.*, Classical many-body model for heavy-ion collisions incorporating the Pauli principle, *Nucl. Phys. A* **282**, 341 (1977).
- [63] J. Randrup, C. Dorso, and S. Duarte, Quasi-classical treatment of the nucleon gas, *J. Phys. Colloques* **48**, C2-143 (1987).
- [64] D. H. Boal and J. N. Glosli, Computational model for nuclear reaction studies: Quasiparticle dynamics, *Phys. Rev. C* **38**, 2621 (1988).
- [65] D. H. Boal and J. N. Glosli, Quasiparticle model for nuclear dynamics studies: Ground-state properties, *Phys. Rev. C* **38**, 1870 (1988).
- [66] K. J. LaGattuta, Multiple ionization of helium clusters by long wavelength laser radiation, *Eur. Phys. J. D* **2**, 267 (1998).
- [67] J. S. Cohen, Multielectron effects in capture of antiprotons and muons by helium and neon, *Phys. Rev. A* **62**, 022512 (2000).
- [68] D. A. Wasson and S. E. Koonin, Molecular dynamics simulations of atomic ionization by strong laser fields, *Phys. Rev. A* **39**, 5676 (1989).
- [69] W. A. Beck, L. Wilets, and M. A. Alberg, Semiclassical description of antiproton capture on atomic helium, *Phys. Rev. A* **48**, 2779 (1993).
- [70] P. B. Lerner, K. J. LaGattuta, and J. S. Cohen, Ionization of helium by a short pulse of radiation: A Fermi molecular-dynamics calculation, *Phys. Rev. A* **49**, R12(R) (1994).
- [71] W. A. Beck and L. Wilets, Semiclassical description of proton stopping by atomic and molecular targets, *Phys. Rev. A* **55**, 2821 (1997).
- [72] J. S. Cohen, Reexamination of over-the-barrier and tunneling ionization of the hydrogen atom in an intense field, *Phys. Rev. A* **64**, 043412 (2001).
- [73] J. S. Cohen, Preliminary results for capture of negative muons and antiprotons by noble-gas atoms, *Hyperfine Interact.* **138**, 159 (2001).
- [74] J. S. Cohen, Comment on laser-assisted formation of antihydrogen, *Phys. Rev. A* **67**, 017401 (2003).
- [75] J. S. Cohen, Capture of negative exotic particles by atoms, ions and molecules, *Rep. Prog. Phys.* **67**, 1769 (2004).
- [76] S. Morita, N. Matsuda, N. Toshima, and K. Hino, Ionization of stabilized helium atoms by proton and antiproton impacts, *Phys. Rev. A* **66**, 042719 (2002).
- [77] This step of the training could have used experimental values; because HF is very accurate for this property, no substantive difference would have been observed.
- [78] In principle, Heisenberg and statistics arguments apply between all species, including the ions. Here we deliberately use the KW

- MDP in its original form to retain a strong connection with the previous literature on MDPs. The development of new MDPs would naturally include a more general form.
- [79] Although all the four parameters could have been varied for the training, we restricted our training to only the core sizes for simplicity and to identify any underlying pattern in the core sizes that could help towards transferability.
- [80] W. A. Beck, L. Wilets, and M. A. Alberg, Semiclassical description of protonium formation in antiproton collisions with molecular hydrogen, *Phys. Rev. A* **74**, 052706 (2006).
- [81] R. Fletcher, *Practical Methods of Optimization* (John Wiley & Sons, Chichester, 2013).
- [82] A. Kramida, Yu. Ralchenko, J. Reader, and NIST ASD Team (2014). NIST Atomic Spectra Database (ver. 5.2), <http://physics.nist.gov/asd> (National Institute of Standards and Technology, Gaithersburg, MD, 2014).
- [83] E. J. McGuire, J. M. Peek, and L. C. Pitchford, Proton stopping power of aluminum ions, *Phys. Rev. A* **26**, 1318 (1982).
- [84] N. R. Arista and P. Sigmund, Stopping of ions based on semiclassical phase shifts, *Phys. Rev. A* **76**, 062902 (2007).
- [85] A. Ojanpera, A. V. Krasheninnikov, and M. Puska, Electronic stopping power from first-principles calculations with account for core electron excitations and projectile ionization, *Phys. Rev. B* **89**, 035120 (2014).
- [86] E. E. Quashie, B. C. Saha, and A. A. Correa, Electronic band structure effects in the stopping of protons in copper, *Phys. Rev. B* **94**, 155403 (2016).
- [87] B. F. Rozsnyai, Electron scattering in hot/warm plasmas, *High Energy Density Physics* **4**, 64 (2008).
- [88] L. G. Stanton and M. S. Murillo, Unified description of linear screening in dense plasmas, *Phys. Rev. E* **91**, 033104 (2015).
- [89] L. de Ferrariis and N. R. Arista, Classical and quantum-mechanical treatments of the energy loss of charged particles in dilute plasmas, *Phys. Rev. A* **29**, 2145 (1984).
- [90] E. J. Heller, Time-dependent approach to semiclassical dynamics, *J. Chem. Phys.* **62**, 1544 (1975).